Real-time thermal management of permanent magnet synchronous motors by resistance estimation

Article *in* IET Electric Power Applications · November 2012

DOI: 10.1049/iet-epa.2010.0232

Published in IET Electric Power Applications
Received on 26th September 2010
Revised on 31st October 2011
doi: 10.1049/iet-epa.2010.0232

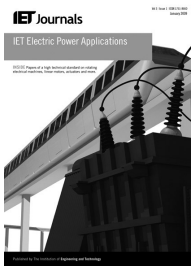

ISSN 1751-8660

Real-time thermal management of permanent magnet synchronous motors by resistance estimation

S.D. Wilson[1] *P. Stewart*[2] *J. Stewart*[2]

[1]*EA Technology, Capenhurst Technology Park, Capenhurst, Cheshire CH1 6ES, UK*
[2]*Faculty of Engineering, University of Lincoln, Lincolnshire LN6 7TS, UK*
E-mail: pstewart@lincoln.ac.uk

Abstract: Real-time thermal management of electrical machines relies on sufficiently accurate indicators of internal temperature. One indicator of temperature in a permanent-magnet synchronous motor is the stator winding resistance. This study applies two current injection techniques to a commercially produced permanent-magnet servomotor, which are applicable under load and cause minimal disturbance to the shaft torque. The current injection techniques applied here enable the temporary boosting of resistive voltage and consequent application to low-resistance, high-voltage machines. The effectiveness of the approach is demonstrated by tracking the change in winding temperature during a 2 h load cycle.

1 Introduction

Brushless permanent-magnet machines have emerged as the preferred electrical machine technology for many applications because of their high specific power and high efficiency. As is common with other types of electrical machine, their output power is usually limited by the maximum operating temperature of key machine components [1]. It is a common, but highly inefficient practice, to design a machine on the basis of a worst-case estimate of the operating conditions, in order to protect against over-temperature. A consequence of this approach results in the machine operating well below its maximum performance for much of its life, particularly in applications with intermittent or unpredictable duty cycles. In such applications, a machine could achieve a transient power rating that is considerably greater than its continuous rating if the thermal capacity of the machine is fully harnessed.

In order to fully exploit the thermal capacity of a machine in applications with variable and often unpredictable duty cycles, monitoring key temperatures within the machine is vital. Temperature monitoring within a machine could be achieved using an array of thermal sensors embedded throughout the machine. One drawback of this approach is that the relationship between the sensor and component temperatures is reliant on the interface properties, particularly in terms of any time-lags introduced. A 'sensorless' approach becomes attractive, whereby estimates of stator coil temperatures can be obtained by tracking changes in the coil resistance, which in turn are derived from terminal voltage and current measurements.

Terminal resistance measurements provide a means of determining average coil temperatures, which can be used as input to a machine-specific thermal model to provide more localised temperature estimates. Winding temperature estimation also provides information for health monitoring, prognostics and real-time thermal management of a machine, for example a real-time variable de-rating to match the peak transient duty cycle.

In practice, tracking resistance changes in permanent-magnet (PM) machines is extremely challenging, particularly in high-efficiency, high-power machines, where the stator resistive voltage drop relative to the net terminal voltage under normal operating conditions is often very small. The experimental machine examined in this paper has a resistive voltage drop at a rated current of just 1.1% of the terminal voltage, with the parameters of Table 1. To provide a temperature resolution as coarse as 10°C in this machine, which represents a realistic objective in order to avoid transient overheating, would require a means of reliably extracting the true resistive voltage component to a resolution of 0.04%. These difficulties are compounded in a practical drive system by the presence of several disturbances in the voltage and current waveforms because of a switching ripple; the action of closed-loop controllers which continually adjust the current to meet some specified commanded motion; the presence of varying degrees of magnetic saturation in the stator, rotor core and rotor saliency.

Notably, resistance estimation methods based on terminal measurements cannot usually provide the precision required for high power PM machines. The method described here is based on intermittent current injection to temporarily boost the resistive voltage contribution, thus increasing the accuracy of measurement. Since the thermal time constant of a large PM machine is many orders of magnitude longer than the duration of the injected pulses, therefore the additional heating effect within the machine is negligible.

2 Stator-winding resistance estimation

This paper presents a report on the practical implementation (and results) of the 'Fixed-Magnitude' method of resistance estimation, whose theory is presented in [2]. The current

Table 1 Nameplate PMSM parameters

Parameter	Symbol	Value
torque constant	K_t	2.08 Nm/A
EMF constant	K_3	1.19 Vs/rad
rated speed	ω_{rated}	314 rad^{-1}
rated continuous power output	P_{cont}	11.9 kW
rated continuous current	I_{cont}	31.9 A RMS
stall current	I_{stall}	117.5 A RMS
maximum phase voltage	V_{ac}	480 V
line-to-line inductance	L_{l-l}	11 mH
rotor moment of inertia	J	0.00841 kg m^2
pole-pairs	p	3
thermal time constant	τ_{th}	2880 s (48 min)
torque due to Coulomb friction	T_c	0.908 N m

injection and signal separation techniques presented in this paper are here applied to a drive system controlling a commercially produced interior permanent-magnet (IPM) motor. The current injection techniques enable the temporary boosting of voltage developed across the winding resistance. Signal separation and resistance estimation algorithms are applied to determine the resistance parameter. There are various reasons why the winding resistance parameter is of interest, which are referred to in the Methods paper [2], including the enhancement of motor-control techniques and estimation of the winding temperature. This research is directed at the latter field, with the estimated resistance being used to determine the estimated winding temperature.

The stator winding of a typical machine consists of several insulated copper coils, whose resistance varies as a function of coil temperature as

$$R_s = R_{s0} + \alpha R_{s0}(T_s - T_0) \quad (1)$$

where R_{s0} is the winding resistance at $T_0{}^\circ$C, R_s is the winding resistance at $T_s{}^\circ$C and α is the temperature coefficient of copper (3.93×10^{-3} per $^\circ$C);

for $R_{s0} = 0.133\ \Omega$ at 25°C and $R_s = 0.183\ \Omega$ at 120°C. Thus, there is a significant change in resistance over an operating temperature range, providing a means of determining the temperature of the stator coils. For a 10°C resolution in the operating temperature range the resistance must be estimated to an accuracy of approximately 5 mΩ. Achieved accuracies of 10 mΩ result in a resolution of 20°C etc.

3 Practical implementation

3.1 Hardware

The methods are implemented on a Kollmorgen BH-824-D' IPM motor of continuous power output 11.9 kW, with nameplate parameters as listed in Table 1. The servomotor possesses near-sinusoidal electromotive force (EMF), the parameters of which EMF are calculated from a recording of the EMF waveform captured using a digital oscilloscope, and the ten frequency components of greatest magnitude are presented in Table 2.

Motor current control is undertaken by a TMS320F2812 Digital Signal Processor (DSP), running space vector pulse-width modulation (SVPWM). The inverter is custom-built around a commercially available three-phase six-switch inverter module, 'Semikron SKiiP 603GD122-3DUW' rated at 900 V and 600 A. The current injection system as

Table 2 Electrical harmonics of the phase-*A* EMF

Harmonic number	Magnitude, % of fundamental
1	100
8	1.61
7	0.35
3	0.22
10	0.16
17	0.14
19	0.11
5	0.10
4	0.07
9	0.06

implemented represents an add-on system that runs on a 'dSPACE 1006' platform with expansion input and output cards for digital and analogue signals (Fig. 1). The estimation takes place offline using currents and voltages recorded during injection by the dSPACE platform. Estimation functions are written for the MATLAB/Simulink environment. The add-on system is implemented to avoid interference with the original drive system, in practice the two systems could be combined.

An implementation of real-time current injection and on-line estimation is achievable if the system is able to buffer voltages and currents in memory. In order to test different procedures, in this application signals were recorded for offline processing.

For the measurement of temperature, thermocouples are attached to the motor stator end-winding and case. As the motor is commercially sourced, the thermocouples could only be attached to the surface of the components and do not directly measure the internal temperature of the components themselves. These measurements were recorded by a 'Labview' data acquisition system. The servomotor is connected to a 75 kW dynamometer for loading and testing.

3.2 Signal processing

Key to the estimation of resistance is the motor currents and voltages. In most three-phase star-connected drive systems, two current sensors are used together with angular position information to determine the axes currents. The axes currents are therefore available in an unmodified drive system. 'LEM LA305-S' closed-loop hall effect sensors with a peak measuring current of ± 250 A, and quoted overall accuracy of $\pm 0.8\%$ are employed in measuring two of the phase currents. Although not the highest accuracy current sensors available, this type of sensor is of a type typically found in drive systems.

Motor voltage may be measured using voltage transducers, or estimated from the output of the current controller or inverter gate signals, in Fig. 1. The Semikron packaged inverter module did not have the gate signals available, so the parameters must be used to estimate the average applied voltage as in [3, 4]. In [5] a sensorless parameter-based method is compared with the transducer measurements, the result being that the estimated voltage at best achieves a 20% root-mean-square (RMS) estimation error (at 20 Hz output frequency) and at worst achieves a 50% RMS estimation error (at 30 Hz output frequency) for a heatsink temperature of 25°C and full load current. The estimation error is a function of the heatsink temperature, output frequency and load current. Since the resistance and

doi: 10.1049/iet-epa.2010.0232

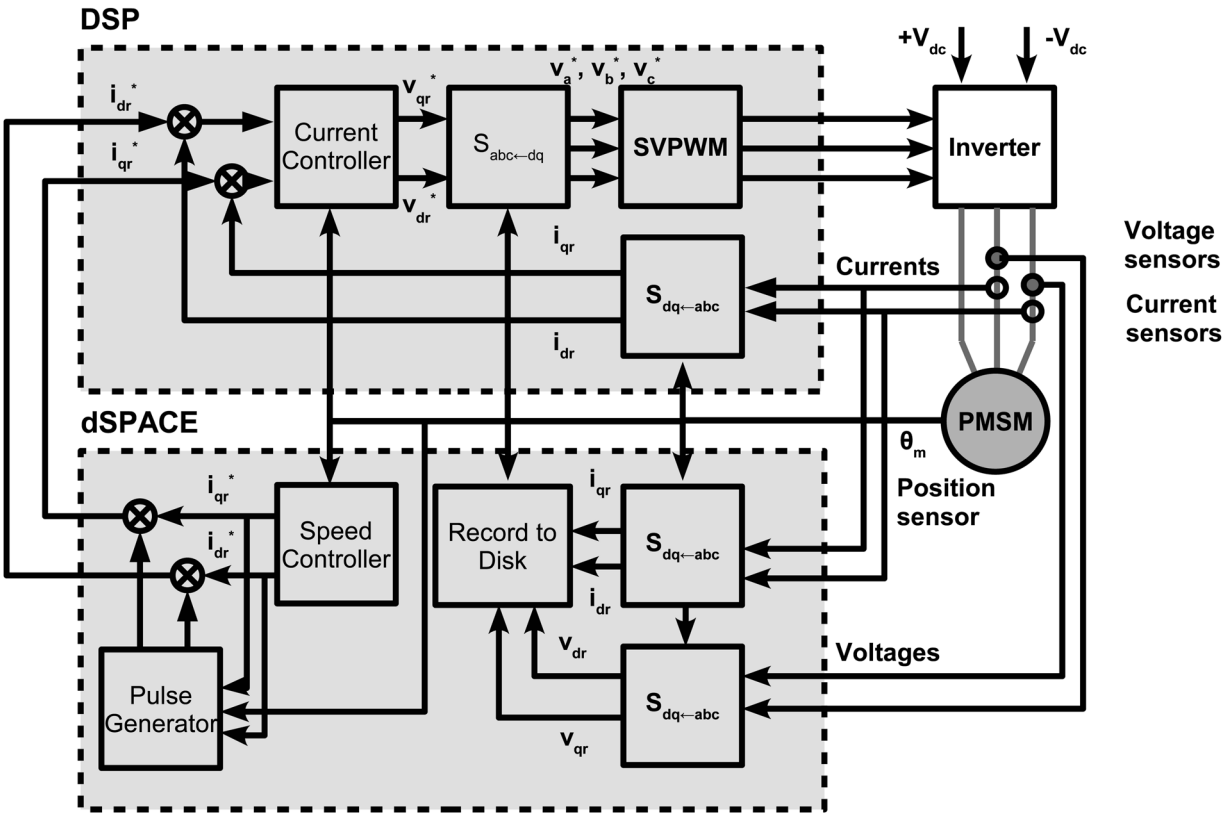

Fig. 1 *Drive system modified to include additional equipment enabling resistance estimation*

temperature variation thereof induces small changes in the voltage, the greatest available voltage precision is required and the measurements are preferred over the estimates.

'LEM LV25-P' voltage transducers are employed to scale the inverter voltages for input to the dSPACE system. These are closed-loop hall-effect devices with a measuring range of ± 400 V, a quoted overall accuracy of $\pm 0.8\%$ and a response time of 40 μs. The transducers were mounted in the motor terminal box. For voltage measurements, a current proportional to the measured voltage is passed through a high precision resistor in series with the promary circuit of the transducer. The chosen transducer displays high accuracy, linearity, low thermal drift and high bandwidth.

3.3 Implementation

Estimation of the resistance depends on voltage and current measurements. Sampling the current measurements at the midpoint of the SVPWM zero vector resolves the fundamental component of the current waveform, and is ripple free. Sampling of the current using this approach is demonstrated in [6]. The SVPWM voltage waveform consists of the application of six discrete voltage vectors per PWM cycle, and contains a high proportion of harmonics compared with the magnitude of the fundamental voltage [7].

The motor control system is augmented with a 'separate' resistance estimating system, in Fig. 1. It was not possible for the dSPACE system to read the sampled voltage and current measurements directly from the DSP, since a compatible communication bus was not available. Both systems are therefore required to sample the input signals. Although sampling in the DSP occurs synchronously to the PWM timers, it does not in the dSPACE system unless a device provides synchronisation. Use of the synchronising device avoids the problem of the dSPACE system making consecutive samples which occur at different times relative to the start of the PWM cycle.

A stand-alone sample-and-hold board has been designed which is triggered by detection of the SVPWM zero vectors. Fig. 2 illustrates the SVPVM vectors that are applied in a section of the rotor angular position $0 < \theta < 60^\circ$. The zero vectors are denoted V_0 or V_7, and either can be used for sampling. The sensor inputs are latched while being digitised by the dSPACE system. The sampling instant relative to the zero vector is tuned using a monostable delay circuit, in Fig. 3. Ideally, sampling should occur at the midpoint of the zero vectors but because of a limitation of the practical rig this could not be achieved. The closest that could be achieved using the signals available from the DSP was to apply a small time delay, $t_1 = 4$ μs. The time period t_2 was set to 50 μs in order for the dSPACE system to sample all the inputs in a single programme cycle time of 67 μs.

All analogue inputs are zero-vector sampled, and anti-aliased with third-order Bessel filters with a cut-off frequency of 5 kHz, which also facilitate low-pass filtering of the PWM voltages. Analogue Bessel filters were chosen since they are characterised by almost constant group delay across the entire passband, thus preserving the wave shape of filtered signals in the passband, allied with ease of implementation. The voltages and currents are sampled at 16-bit precision, with full-scale deflections set to 400 V and 200 A. These were the highest precisions available at 15 kHz sampling rate (equal to the SVPWM switching frequency), giving at least in principle, voltage and current resolutions of 12.2 mV and 3 mA.

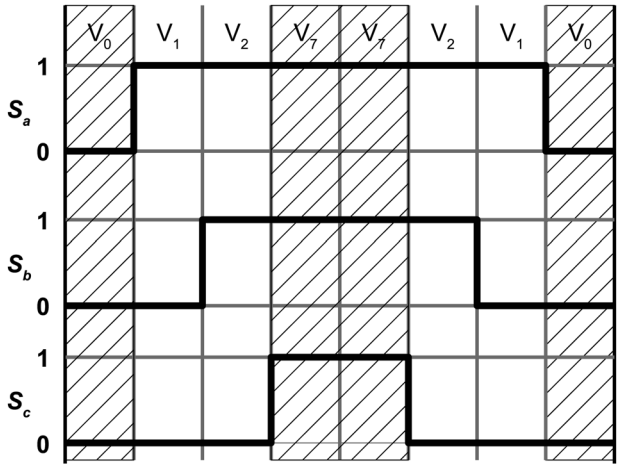

Fig. 2 *Example per-carrier cycle switching sequence for switches S_a, S_b, S_c, $0 < \theta < 60^\circ$, where the zero vectors are hatched and denoted V_0, V_7*

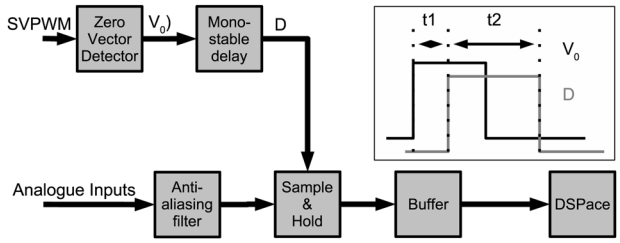

Fig. 3 *Schematic diagram of zero-vector sampling system and representation of delays t_1, t_2*

4 Permanent-magnet synchronous motor (PMSM) *dq*-axis model

The concept of resolving machine armature quantities into two rotating components, one aligned with the field axis, the direct-axis component (d) and one in quadrature with the field axis, (q) is a well-established and widely used means of analysing electrical machines. These components, which are stationary with respect to the rotor, are referred to as being in the rotor-stationary frame of reference (qdr). When transferred to the stator-stationary frame of reference, they are referred to as being in the stator-stationary frame of reference (qds).

The transformation itself can be represented in terms of the electrical angle between the rotor direct-axis and the stator phase-a axis [8]. Letting S represent the quantity to be transformed (current, voltage or flux), the transformation can be written in matrix form using Park's transformation as

$$\begin{bmatrix} S_d \\ S_q \\ S_0 \end{bmatrix} = \frac{2}{3}\begin{bmatrix} \cos(\theta) & \cos(\theta-2\pi/3) & \cos(\theta+2\pi/3) \\ -\sin(\theta) & -\sin(\theta-2\pi/3) & -\sin(\theta+2\pi/3) \\ 1/2 & 1/2 & 1/2 \end{bmatrix} \times \begin{bmatrix} S_a \\ S_b \\ S_c \end{bmatrix} \quad (2)$$

where S_d, S_q and S_0 denote the d-axis, q-axis and zero-sequence components of the transformed phase quantities S_a, S_b and S_c.

An equivalent inverse transform exists which transfers the $dq0$ quantities into stator three-phase quantities. Under balanced conditions there are no zero-sequence components. When the PMSM three-phase motor equations are also transformed into the rotor reference frame the motor variables may be represented by the following matrix

$$\begin{bmatrix} v_{dr} \\ v_{qr} \end{bmatrix} = \begin{bmatrix} R_s & -\omega L_q \\ \omega L_d & R_s \end{bmatrix}\begin{bmatrix} i_{dr} \\ i_{qr} \end{bmatrix} + \begin{bmatrix} L_d & 0 \\ 0 & L_q \end{bmatrix}\frac{d}{dt}\begin{bmatrix} i_{dr} \\ i_{qr} \end{bmatrix} + \begin{bmatrix} 0 \\ K_e\omega_m \end{bmatrix} \quad (3)$$

where v_{dr} and v_{qr} are the direct and quadrature axes voltages in the rotor reference frame, i_{dr} and i_{qr} are the direct and quadrature axes currents in the rotor reference frame, R_s is the stator resistance, L_d and L_q are the non-saturated direct and quadrature axis inductances, K_e is the back-EMF constant, ω is the electrical frequency and ω_m is the rotor angular velocity in radians per second.

5 Three-system representation of current injection

When the motor is running as part of a drive system, it generates a voltage that is defined by the EMF waveform, axes currents and motor parameters such as L_d, and L_q. The voltages are described as functions of current by the PMSM voltage equation denoted G_1

$$\begin{bmatrix} v_{dr} \\ v_{qr} \end{bmatrix} = \begin{bmatrix} R_s & -\omega L_q(i_{dr}, i_{qr}) \\ \omega L_d(i_{dr}, i_{qr}) & R_s \end{bmatrix}\begin{bmatrix} i_{dr} \\ i_{qr} \end{bmatrix} + \begin{bmatrix} L_d(i_{dr}, i_{qr}) & 0 \\ 0 & L_q(i_{dr}, i_{qr}) \end{bmatrix}\frac{d}{dt}\begin{bmatrix} i_{dr} \\ i_{qr} \end{bmatrix} + \begin{bmatrix} k_d(\theta)\omega_m \\ k_q(\theta)\omega_m \end{bmatrix} \quad (4)$$

where k_d, k_q are EMF generators and the axes inductances are described as functions of the axes currents. The EMF generators represent the variation of the EMF with respect to rotor position and are described in more detail in Section 6.

The voltage of the motor during current injection is the sum of the normal, and 'injection function', G_2 voltages. By manipulation of (4) with d-axis injection current i_{idr} and zero q-axis injection current, the G_2 system equation is formed

$$v_{dr} = R_s i_{idr} + L_d\frac{d(i_{idr})}{dt} \quad (5)$$

$$v_{qr} = \omega L_d i_{idr} \quad (6)$$

The G_1 and G_2 systems describe the operation of the drive system, provided the operation of each system does not affect the parameters of the other. In practice, when current is injected (by way of the injection function) it influences the parameters describing the G_1 and G_2 systems through magnetic saturation and cross-coupling effects, thus, the function, G_1, voltage changes. A measurement of the q-axis inductance L_q with respect to d-axis current for this machine (obtained by sinusoidal excitation on the q-axis with supply of bias current on the d-axis, in a similar manner to Stumberger *et al.* [9]) shows that saturation

doi: 10.1049/iet-epa.2010.0232

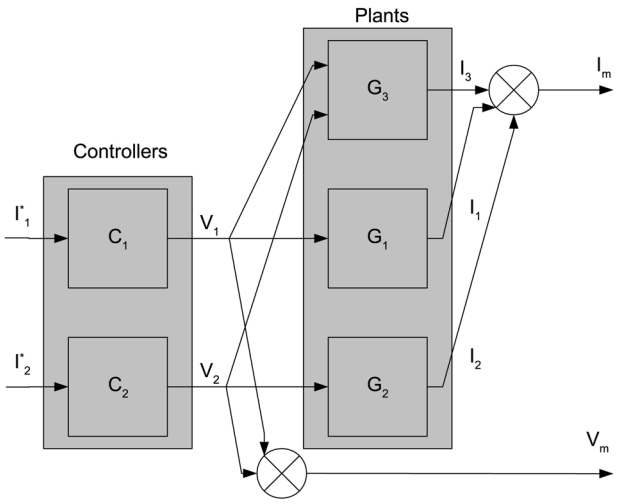

Fig. 4 *Motor normal and injection functions with parameter change compensation*

accounts for a significant change in the L_q parameter; between the $\pm FA$ injection current with the bipolar method, and the zero, FA currents of the unipolar method, in Fig. 5. The voltage response of this parameter change can be represented by the use of a third system, G_3, whose output voltage is a function of the normal operating currents i_{dr}, i_{qr} and the injection current i_{idr}. A representation of the interaction between the three systems is shown in Fig. 4; where I_1^* and I_2^* are demanded currents for the G_1 and G_2 systems, respectively, I_1, I_2 and I_3 are current components of the G_1, G_2 and G_3 systems, respectively, V_1, V_2 are the controller output voltages, with $V_{\rm m}$ and $I_{\rm m}$ being the measured voltages and currents.

The L_q parameter change is responsible for part of the voltage represented by the G_3 system. The system also generates a voltage in response to changes in the L_d, k_d and k_q parameters. Such changes occur as a result of the dependence of motor parameters on motor currents and speed. The voltages generated by all three systems sum to produce the measured voltage $V_{\rm m}$. Controller C_1 controls the motor function, and C_2 controls the current injection function.

Theoretical calculation of the G_3 system equations requires a detailed model, taking into account magnetic saturation, to be available. Such a model could be produced using materials data and finite-element analysis, but is dependent on materials data and dimensional information. This information was not available for the motor under study. Therefore an empirical method is preferred, whereby resistance estimates are obtained at different operating points (of torque, speed) and compared with the 'true' winding resistance obtained by measurement of the winding temperature. The difference between the two resistances is assumed to be because of the G_3 system, and the approximation of these voltages is described in Section 7.2.

6 EMF waveform

The EMF is the largest component of motor voltage at rated speed and torque output. According to the parameters of Table 1, the EMF comprises 89% of the terminal voltage at rated speed and torque. As described in Part 1, the EMF is separated from the current injection signals by setting the electrical angle between injection pulses to $\Delta\theta = np\pi$, where n is an integer number of revolutions. The minimum choice of n is required to minimise the time between injection pulses, and can be found by analysing the EMF waveform.

The EMF waveform is recorded at 1000 RPM using a dynamometer and digital oscilloscope. The dq-axes EMFs are calculated and presented in Fig. 6, where the q-axis EMF is normalised by subtraction of the mean EMF.

Fig. 6 shows that the EMF varies as a function of mechanical and electrical positions. The reason for variation with respect to mechanical position has not been investigated, but is assumed to be because of features of manufacturing or electrical abuse of the motor. Therefore $\Delta\theta = 2p\pi$ is required so that successive injection pulses occur at identical mechanical positions. The parameters of the EMF generator $k_d(\theta)$, that forms part of (4) can be found from the Fourier coefficients of the d-axis EMF, Table 3. Note that these parameters are not required to separate the motor voltages from the injection voltages, but are presented to illustrate the significant magnitude of the harmonic voltages compared with the resistive voltage magnitude. That is, the $N_d = 1$ harmonic generates a voltage which is equivalent to 42% of the injection voltage FR_s at $F = 50$ A and $R_s = 0.13\ \Omega$.

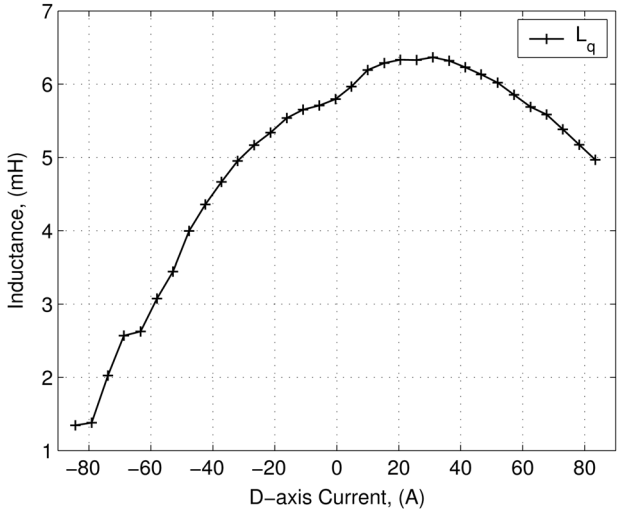

Fig. 5 *Measured q-axis inductance as a function of d-axis current*

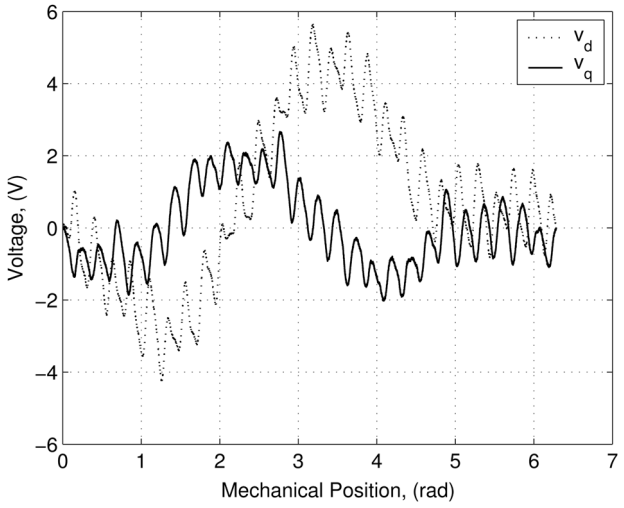

Fig. 6 *Normalised dq-Frame EMF*

Table 3 Ten largest Fourier coefficients of *d*-axis EMF at 1000 RPM

Harmonic number, N_d	Magnitude, V/kRPM	Angle, °
1	2.7327	141.0
2	1.5494	1.5
27	0.7795	90.4
0	0.7425	0.0
18	0.4044	−89.2
54	0.2525	−105.2
6	0.1108	42.3
4	0.0973	−136.8
26	0.0845	37.4
28	0.0771	−37.7

7 Processing system for resistance estimation

A schematic of the processing functions required to generate resistance estimates is presented in Fig. 7. First, the measured currents and voltages must be converted from functions of time to functions of position. An interpolation is required to form output data with a constant 360 points per electrical revolution. This enables the combination of measurements taken during successive mechanical revolutions, and separation of the EMF from the injection signal as described in [2]. Next, the data sets are split into two streams (P1, P2), each stream containing the signals during the application of each pulse. These two streams are required to enable the normal function signals ($\Sigma(v, i, t)$) to be calculated by $P1 + P2$, and the injection function signals ($\Delta(v, i, t)$) to be calculated by $P1 - P2$. The $\Delta(v, i, t)$ signals are processed for the compensation of parameter variation by the G_3 compensator.

The current injection methods consist of applying two current pulses. The C_2 controller (Fig. 4) applies the unipolar or bipolar method by changing the magnitude of each pulse accordingly. The polarities of the bipolar current injection pulses are displayed in Fig. 8. The angular definition of the pulses is covered in Part 1.

7.1 Post-processing the resistance estimate

Temperature estimation requires a single value to be chosen for the resistance. The single value is chosen by taking the mean of $\hat{R}_s$ over which time the injection current demand magnitude is equal to F (the window period current is not used for estimation). A small time is allowed to elapse after the application of each current pulse while the voltage settles, and the estimated resistance recorded during this time is not included.

A single 'preferred' value of resistance is thus chosen. For the data presented in Fig. 15, this preferred value is 0.127 Ω.

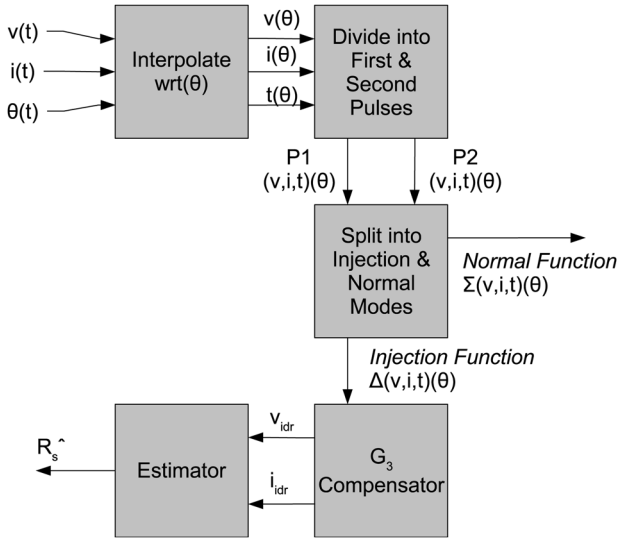

Fig. 7 *Schematic of processing functions for resistance estimation*

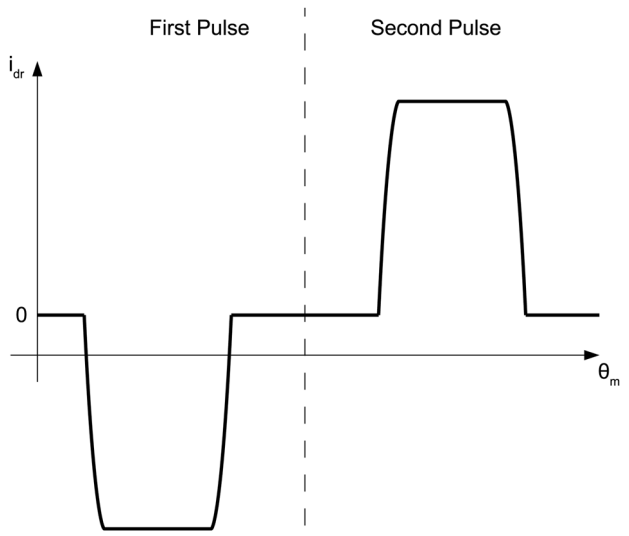

Fig. 8 *Bipolar current injection pulses*

7.2 G_3 system compensation

The G_3 system produces a voltage that is dependent on the change in motor parameters between the first and second injection current pulses. For the bipolar method, the *d*-axis current is defined by the injection current magnitude as $\pm FA$. The *q*-axis current also changes between the pulses because of the influence of the cross-coupling voltages. Both the axes currents influence the axes inductances via magnetic saturation and therefore provide sample equations for the G_3 system. For the bipolar method

First pulse:

$$i_{dr}(\theta_1) = -F \tag{7}$$

$$i_{qr}(\theta_1) = i_{qr} - \Delta i_{qr} \tag{8}$$

$$v_{dr}(\theta_1) = -FR_s - \omega L_q(-F)(i_{qr} - \Delta i_{qr}) \tag{9}$$

Second pulse:

$$i_{dr}(\theta_2) = F \tag{10}$$

$$i_{qr}(\theta_2) = i_{qr} + \Delta i_{qr} \tag{11}$$

$$v_{dr}(\theta_2) = FR_s - \omega L_q(F)(i_{qr} + \Delta i_{qr}) \tag{12}$$

where i_{qr} is the *q*-axis mean current over both pulses, and θ_1,

doi: 10.1049/iet-epa.2010.0232

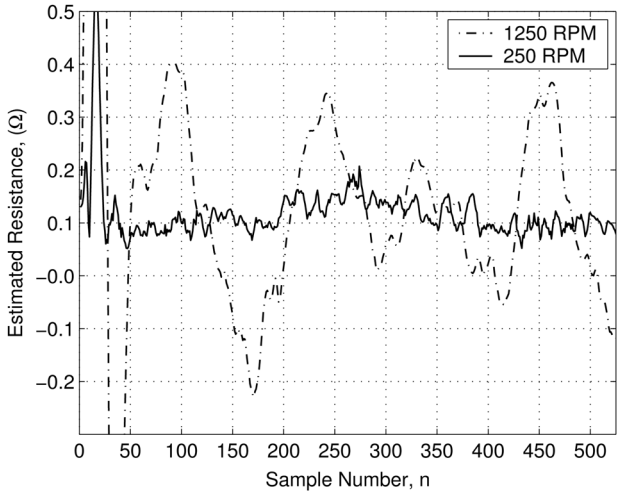

Fig. 9 *Effect of the G_3 signal on the estimated resistance waveform*

θ_2 are ranges of angles for the $P1$ and $P2$ pulses. The voltage difference between the pulses is computed as

$$\Delta v_{dr} = v_{dr}(\theta_2) - v_{dr}(\theta_1)$$
$$\ldots = 2FR_s + \omega(L_q(F) - L_q(-F))i_{qr} \quad (13)$$
$$- \omega(L_q(F) + L_q(-F))\Delta i_{qr} \quad (14)$$

where the last two terms are proportional to speed. The G_3 system voltage is thus proportional to speed. The increase in G_3 voltage with speed is demonstrated in Fig. 9, which compares the determined injection voltage at 250 RPM with that at 1250 RPM measured from the experimental rig.

The formula is simplistic in that it defines the G_3 voltage as a function of inductance variation because of d-axis saturation only. In practice, the inductances are functions of both axes currents in (4), and Δi_{qr} is dependent on the current controller's response to the cross-coupling voltages. Owing to the uncertainty created in the inductance values by these currents, an empirical method is preferred to calculate the values of the constants K_1, K_2 in the following equivalent equation to (14)

$$\Delta v_{dr} = 2FR_s + \omega K_2 i_{qr} + \omega K_1 \quad (15)$$

To calculate K_1 requires K_1 and K_2 to be set to zero and resistance estimates to be obtained over a speed range. During this test the motor was run with no loading other than frictional forces. The end-winding temperature was recorded and used to calculate the end-winding resistance. This is assumed to be the value of the winding resistance, and the innovation (difference) between this value and the estimated resistance is displayed in Fig. 10 (Table 4).

The innovation increases with speed, approximated linearly by the fit line Fit 1, giving $K_1 = 4 \times 10^{-5}$. Note that the linear fit for K_1 has least error around the 250 RPM mark.

To calculate K_2, resistance estimates are obtained with the speed fixed at 1000 RPM, with $K_1 = 4 \times 10^{-5}$ and $K_2 = 0$. Resistance estimates are obtained over a range of load torques, and the innovation against q-axis current is calculated and displayed in Fig. 11. The value of K_2 is found from the linear fit line as 4×10^{-3}. The K_1 and K_2 values could be determined as functions of speed and current, potentially reducing the error in linearly

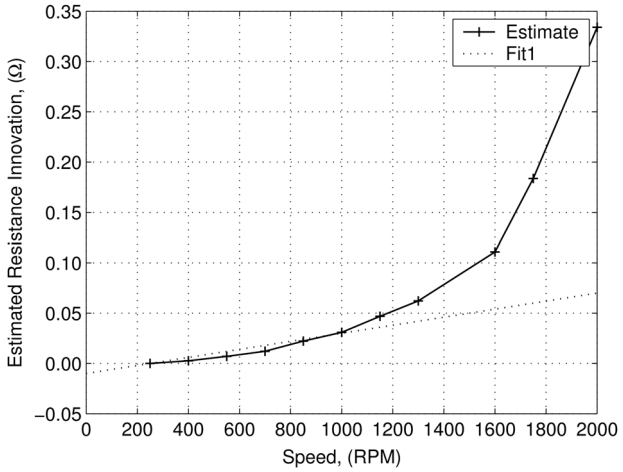

Fig. 10 *Determination of the K_1 value*

approximating the values. The process of determining the coefficients is schematically presented in Fig. 12. However, in applying this method, care must be taken that the innovation at every operating point is accurately computed. More accurate computation could potentially be provided by recording temperatures from a network of thermocouples embedded in the stator winding instead of the single-end-winding thermocouple.

8 Experimental results

The presented results are obtained using the practical setup as described in Section 3. To gauge the performance of the estimation scheme, the different configurations of current injection are tested under various loads and speeds. The

Table 4 Symbol table

Symbol	Parameter
Δ	change in a parameter
θ	electrical rotor position
θ_F	angle of injected current vector (elec)
ω	electrical frequency
ω_m	mechanical (shaft) frequency
i_{dr}	d-axis current, rotor reference frame
i_{qr}	q-axis current, rotor reference frame
I_1	G_1 system current
I_2	G_2 system current
I_3	G_3 system current
I_m	measured current
k_d	EMF constant for d-axis
k_q	EMF constant for q-axis
L_d	D-axis inductance
L_q	Q-axis inductance
N_d	D-axis EMF harmonic number
R_s	stator resistance
S_a	switching signal for inverter phase-A
S_b	switching signal for inverter phase-B
S_c	switching signal for inverter phase-C
t_1	zero-vector sampling delay 1
t_2	zero-vector sampling delay 2
v_{dr}	d-axis voltage, rotor reference frame
v_{qr}	q-axis voltage, rotor reference frame
$V_0 - V_7$	SVPWM vectors
V_m	measured voltage

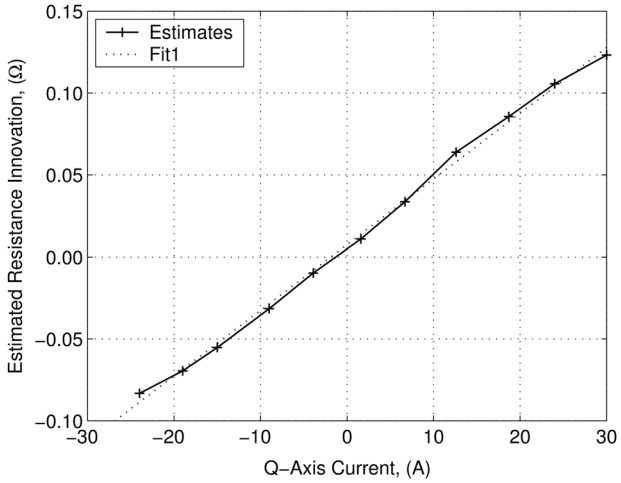

Fig. 11 *Determination of the K_2 value*

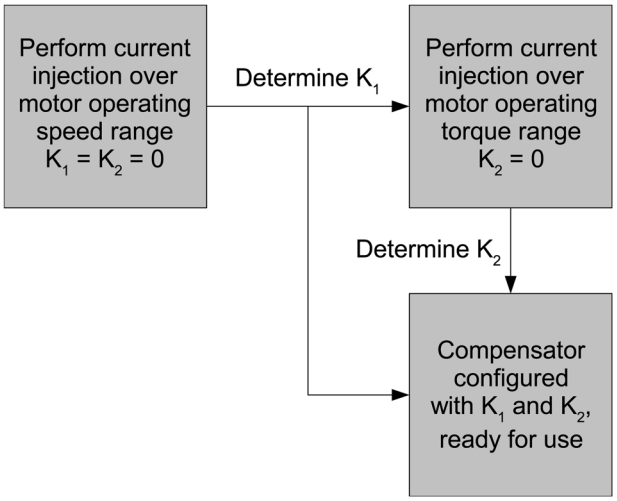

Fig. 12 *Process to determine K_2 and K_2 coefficients*

current injection pulse train consists of sets of current injection pulses with centre angles $\theta_c = [0, 120, 240]^\circ$. A single estimate is formed from each set of pulses, with 50 sets being used to calculate the mean and standard deviation of the estimates at each operating point. The frequency of resistance estimates was set at one estimate (injection of one set of pulses) per second.

8.1 Current pulses and speed disturbance

A single set of current pulses is displayed for the bipolar method, in Fig. 13. The six-pulse i_{dr} injection current is clearly defined, and the corresponding i_{qr} current displayed. Although q-axis current is not demanded by current injection, transiently 40% of the i_{dr} current magnitude is generated because of imperfect current decoupling. As the i_{dr} current flows through the motor, it generates a cross-coupling voltage on the q-axis. The response of the current controller and inverter to this voltage defines the q-axis current, which is the cause of a small amount of speed deviation, in Fig. 14.

8.2 Resistance estimates

The resistance estimate for the current pulses displayed in Fig. 13 is shown in Fig. 15, where the estimates with centre

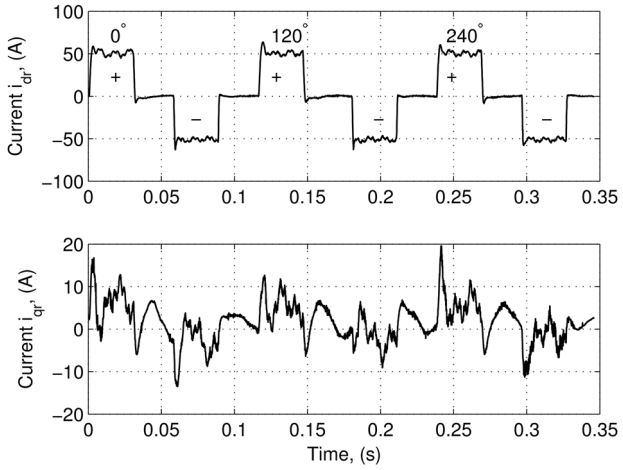

Fig. 13 *i_{dr} current pulses and coupled i_{qr} current, bipolar method*

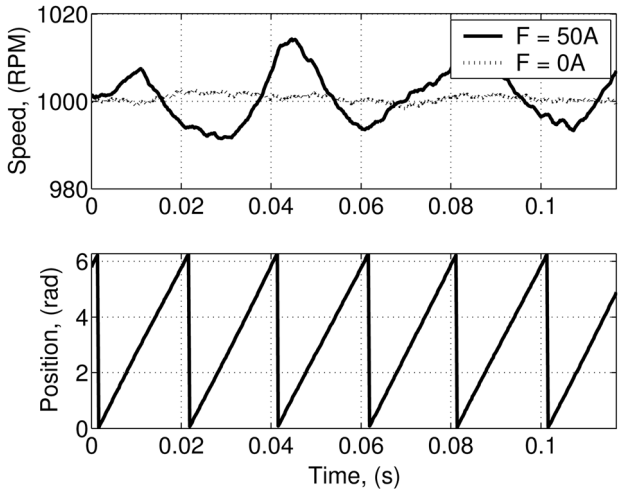

Fig. 14 *Effect of i_{qr} disturbance on speed*

angles [0, 120, 240]° are labelled 1, 2 and 3. A small number of samples elapse after each pulse's initial application during which the resistance is over-estimated (samples 0–50 for Estimate 1). The estimate periodically becomes negative, a result of the slightly varying axes

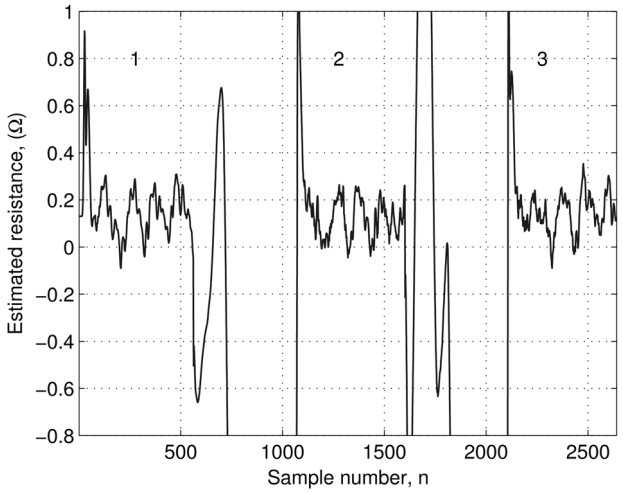

Fig. 15 *Resistance estimate comprising three applications of bipolar method at 1000 RPM*

doi: 10.1049/iet-epa.2010.0232

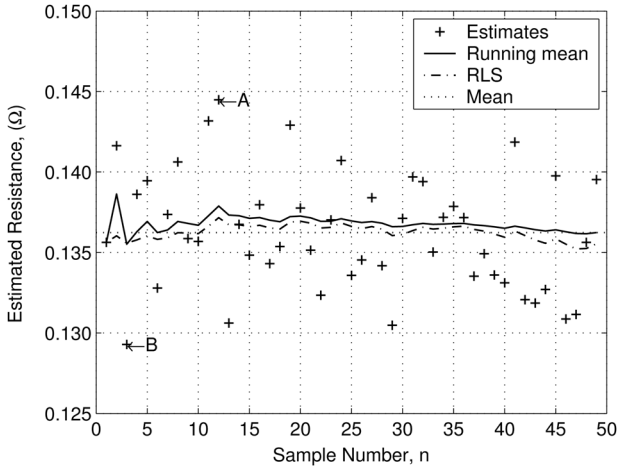

Fig. 16 *Convergence of estimates: A = max, B = min*

currents during injection. The estimated resistance also becomes unreliable immediately after the end of the current pulse (samples >500 for Estimate 1). These periods are ignored when calculating the mean estimated resistance, which is 0.129 Ω for this set of pulses.

Fifty resistance estimates consisting of the bipolar method applied for a period of 540° were taken to demonstrate convergence to a mean value (Fig. 16). The standard deviation of the estimates is 3.6 mΩ, and three standard deviations are within 8% of the mean value. The nominally similar estimates labelled A, B are shown in more detail in Fig. 17. The estimates have similar periodic features but differ in their mean values by 15 mΩ.

The difference in the mean values cannot be caused by winding resistance changes, since the temperature changes slowly. It is proposed that a mechanism exists whereby parameter change between the two estimates is responsible for an error in determining the injection signals $\Delta(v, i, t)$. One mechanism that causes speed and current change is the actions of current and speed controllers on their respective measurements.

The motor current and voltage must be controlled in order to satisfy demanded torque output and speed. Owing to the inaccuracies of sensors, existence of time-lags and mathematical approximations required to fit a current controller to a drive system, current control will be imperfect. The exhibited features are speed, torque and

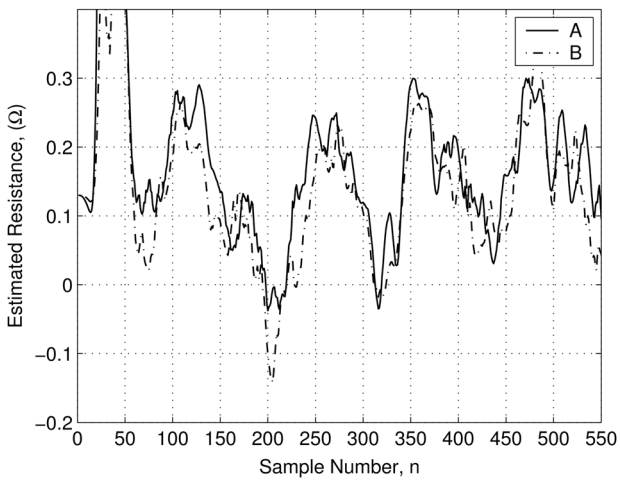

Fig. 17 *Comparison of estimates A and B*

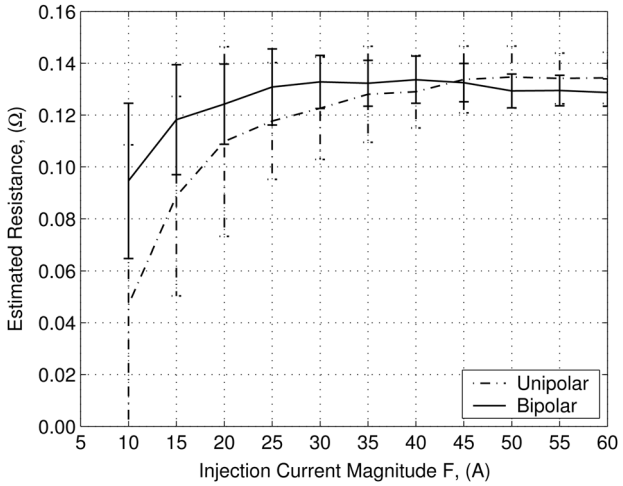

Fig. 18 *Dependence of the mean and standard deviation of the estimates on the injection current magnitude*

voltage deviations which change machine parameters so that the hypothesis of null change between, and within, periods of current injection is loosely applicable. Improvements in current control have the potential to reduce current ripple and parameter change, in general requiring modification to the current control [10–12].

8.3 Evaluation of methods

The bipolar and unipolar methods are compared by applying each method at 1000 RPM and without dynamometer loading. The methods are applied with increasing current magnitude, from 10 to 60 A. Fifty resistance estimates at each magnitude of injection current are processed to calculate the mean and standard deviation of the estimated resistances, in Fig. 18. The mean resistance is represented by the solid line, the upper and lower bars represent the value of resistance one standard deviation above and below the mean, respectively.

For each method the mean value changes as the injection current magnitude is increased, whereas the standard deviation reduces. The reduction in deviation is due to the increase in resistive voltage magnitude FR_s compared with the sources of error outlined in the previous section. Therefore the standard deviation reduces, and the resistance estimates become increasingly accurate as the injection current magnitude F increases to a point, in Fig. 18.

For a given current magnitude F, the standard deviation of the unipolar method is approximately twice that of the bipolar method. The increased confidence in the value of the resistance is due to the generation of twice the resistive voltage (after the $P1-P2$ operation) per ampere of injection current magnitude.

8.4 Resistance estimation accuracy across a speed range

The accuracy of resistance estimation across a speed range is assessed by taking 50 estimates at each 125 RPM speed step, from 250 to 2000 RPM. The temperature of the end winding was recorded over the length of the test in order to provide a thermally derived estimate of winding resistance against which the resistance estimation scheme is compared, in Fig. 19. The mean of the estimated resistance remains within 10% (25°C) of the winding resistance until

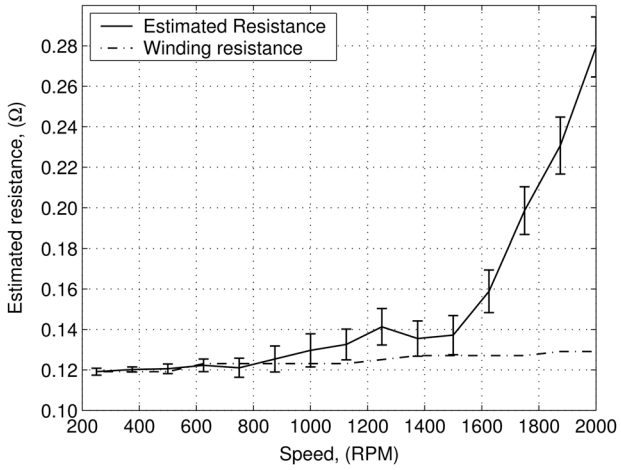

Fig. 19 *Effect of machine speed on estimated resistance*

1250 RPM. Note that the winding resistance is inferred from thermocouple temperature measurement at the surface of the end-winding, which was the only accessible part of the winding bundle. Inferring the winding resistance in this manner cannot account for the end-winding temperature being different from the average temperature of the whole winding. The winding resistance should not be considered accurate. However, the trend of a slowly changing temperature is considered common to the end-winding and the winding as a whole by virtue of their connection.

Above 1500 RPM the estimate becomes inaccurate because of the error in linearly approximating the G_3 system voltage, whose magnitude increases substantially above 1500 RPM, in Fig. 10. With the practical setup as described this limited the speed range for resistance estimation to $\omega_{max}/2$. The speed range could in theory be extended by representing K_1 as a function of speed rather than a linear approximation as displayed in Fig. 10, but care must be taken in obtaining accurate estimates of the winding resistance.

8.5 Accuracy across a torque range

Fifty estimates are taken at each torque setting, with motor q-axis currents in the range -25 to 30 A (-78 to 94% I_{cont}). The estimates are processed to determine the mean and standard deviation of the estimated resistances, in Fig. 20. The mean of the estimates shows deviation up to

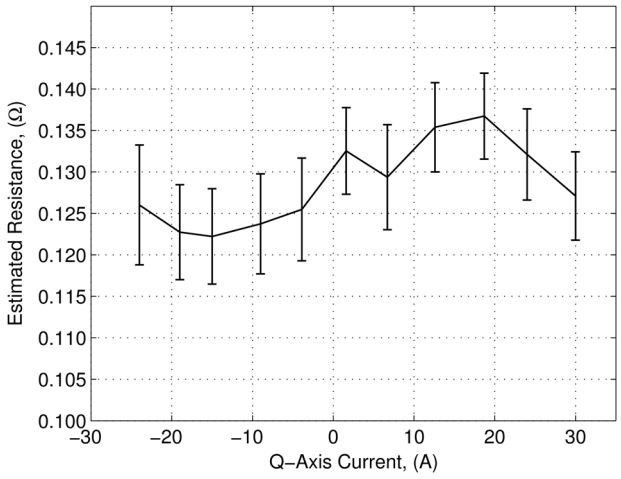

Fig. 20 *Effect of load torque on estimation accuracy*

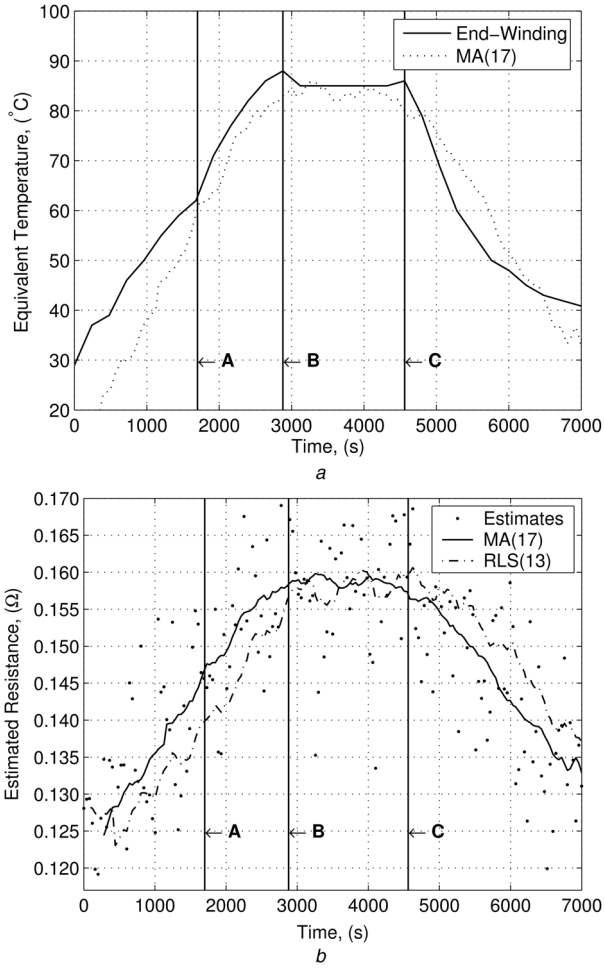

Fig. 21 *Estimated resistance and measured temperature over 2 h load cycle*

a Temperature estimates
b Resistance estimates

$\pm 5.7\%$ of the average resistance value, equating to an uncertainty in temperature of $\pm 14^{\circ}$C. The variation in value is due to the different machine inductances at difference levels of q-axis current. Hence, the accuracy of resistance estimation is again dependent on the G_3 system compensation. The accuracy across the torque range could in theory be improved by storing K_2 as a function of q-axis current rather than a linear approximation as displayed in Fig. 11. In this case, due care must be taken in establishing precise winding resistance.

8.6 Temperature estimation

The motor was thermally cycled by dynamometer control of the load torque. Over a 2 h period, the motor was loaded to 50 A q-axis current (150% rated, origin $\rightarrow A$) for 30 min, 65 A (200% rated) until the end-winding measured 90° ($A \rightarrow B$) and the temperature stabilised at 85% for 30 min by loading to $\sim$40 A (125% rated, $B \rightarrow C$). The load was then reduced to zero and the motor cooling assisted with a fan until the remaining time elapsed. The end-winding temperature is displayed in Fig. 21*a*. During this period, motor load was temporarily reduced to zero every 40 s to permit current injection. Note that it is not prudent to induce large magnitude d-axis currents under high torque output because of the risk of demagnetisation. The estimates are processed off-line by a 17-point moving

doi: 10.1049/iet-epa.2010.0232

average filter 'MA(17)' and recursive least-squares filter with forgetting factor 1/13, 'RLS(13)'. These processing methods are compared in Fig. 21*b*. Note that these filters suffer from end-effects at the start and end of the *x*-axis.

RLS(13) lags MA(17), and is prone to oscillation in the $B \rightarrow C$ region. Increasing the forgetting factor removes the oscillations, but at the cost of a greater time lag. Between the origin and point 'A' the initial high rate of winding temperature increase is mirrored in the resistance increases, followed by a period of lower-rate heating. Between points 'A' and 'B' the winding temperature rises quickly as the load is increased. The filtered estimates also rise at high rates.

Between points 'B' and 'C' the winding temperature remains constant at 85°. MA(17) best approximates the constant temperature, whereas the RLS(13) filter is prone to deviations. From point 'C' the exponential cooling is best detected by MA(17), with less time-lag than RLS(13).

The resistance estimated from the moving average filter is converted to an equivalent temperature using the winding resistance of 0.129 Ω at 25°C, and presented with the measured end-winding temperature for comparative purposes, in Fig. 21*a*. Note that the end-windings compose only a section of the winding, are not in contact with the back-iron and attain a different temperature to that of the winding as a whole.

9 Conclusion

An evaluation of the fixed-magnitude resistance-estimating methods proposed in [2] is presented. Similar to other signal injection methods, the motor load current and resistance sense currents are decoupled. Since the motor does not have to be loaded to enable resistance estimation, it may take place on-demand. The new methods, unlike other signal injection-based methods; do not require the motor star point to be available, and there is no direct generation of pulsating torque. Hence, there is greater scope for application.

These features are avoided in the new technique by separating the sense current and voltage from the load current and voltage; not by provision of a different circuit for the sense current, nor by provision of a frequency difference between the sense and load currents. Instead, the separation is achieved by hypothesising that change in the motor parameters is negligibly small between one revolution and the next. The sensing signals are computed in the current and voltage differences between revolutions with, and without sense current; or between revolutions with opposite polarities of sense currents. Digitally controlled, inverter-driven drive systems require augmenting with the necessary voltage measuring equipment, estimation functions and additional inverter VA (if estimation is desired during high-load periods) to enable the benefits of resistance and temperature estimation.

A chief advantage of the method is the elimination of the use of parameters in describing motor voltages. As the parameters are not estimated, the computational requirements can be reduced. The only parameters explicitly required are two experimentally determined values K_1, K_2, although the simple tuning process outlined in this paper requires further work to improve and identify its applicability to different machines.

The methods have been tested on a commercially produced servomotor that exhibits significant change in the inductance parameter with current magnitude. The load current flowing through the machine resistance at full load develops a voltage less than 1.1% of the EMF at rated speed. This feature creates difficult conditions for resistance estimating methods.

In practice, the estimated resistance is sensitive to speed and torque variations, which is reflected in the estimations for the machine described in this paper. Uncertainty in the true value of the resistance is reduced by using multiple applications of the method, which are then processed by a moving-average filter. The filtered estimates are accurate enough to be used for temperature estimation, demonstrated through a thermal cycle of the test motor. In certain areas of the machine torque and speed envelope, it is not possible to inject the required sense current, because of the available inverter voltage or consideration of de-magnetisation effects. However, at least some of these regions are eminently suitable for complementary methods based on load-current sensing. In conjunction with such methods, the overall solution is able to provide the on-demand resistance estimation that enables the real-time thermal management of PMSMs.

10 Acknowledgment

S.D. Wilson was supported by a grant from the Engineering and Physical Sciences Research Council (EPSRC) and a Co-operative Award in Science and Engineering (CASE) provided by Rolls-Royce PLC. Technical support, and the hardware used in this research were provided by the EPSRC Project Zero-Constraint Free Piston Energy Converter, Grant Number: GR/S97507/01.

11 References

1 Bonnet, A.H.: 'Root cause ac motor failure analysis', *IEEE Trans. Ind. Appl.*, 2000, **36**, (5), pp. 1435–1448
2 Taylor, B., Wilson, S., Stewart, P.: 'Methods of resistance estimation in permanent magnet synchronous motors for real-time thermal management', *IEEE Trans. Energy Convers.*, 2010, **25**, pp. 698–707
3 Kim, H.-W., Youn, M., Cho, K., Kim, H.-S.: 'Nonlinearity estimation and compensation of pwm vsi for pmsm under resistance and flux linkage uncertainty', *IEEE Trans. Control Syst. Technol.*, 2006, **14**, (4), pp. 589–601
4 Guerrero, J., Leetma, M., Briz, F., Zamorrón, A., Lozenz, R.: 'Inverter nonlinearity effects in high-frequency signal-injection-based sensorless control methods', *IEEE Trans. Ind. Appl.*, 2005, **41**, (2), pp. 618–626
5 Yu, X., Dunnigan, M., Williams, B.: 'Phase voltage estimation of a pwm vsi and its application to vector-controlled induction machine parameter estimation', *IEEE Trans. Ind. Electron.*, 2000, **47**, (5), pp. 1181–1185
6 Blasko, V., Kaura, V., Niewiadomski, W.: 'Sampling of discontinuous voltage and current signals in electrical drives: a system approach', *IEEE Trans. Ind. Appl.*, 1998, **34**, (5), pp. 1123–1130
7 Holmes, D., Lipo, T.: 'Pulse-width modulation for power converters' (IEEE Press, 2003)
8 Fitzgerald, A., Charles Kingsley, J., Umans, S.D.: 'Electric machinery' (McGraw-Hill, 2003)
9 Stumberger, B., Stumberger, G., Dolinar, D., Hamler, A., Trlep, M.: 'Evaluation of saturation and cross-magnetization effects in interior permanent-magnet synchronous motor', *IEEE Trans. Ind. Appl.*, 2003, **39**, (5), pp. 1264–1271
10 Angelo, C.D., Bossio, G., Solsona, J., García, G., Valla, M.: 'Mechanical sensorless speed control of permanent-magnet ac motors driving an unknown load', *IEEE Trans. Ind. Electron.*, 2006, **53**, (2), pp. 406–414
11 Grcar, B., Cafuta, P., Stumberger, G., Stankovic, A.: 'Control-based reduction of pulsating torque for pmac machines', *IEEE Trans. Energy Convers.*, 2002, **17**, (2), pp. 169–175
12 Ferretti, G., Magnani, G., Rocco, P.: 'Modeling, identification, and compensation of pulsating torque in permanent magnet ac motors', *IEEE Trans. Ind. Electron.*, 1998, **45**, (6), pp. 912–920